

## X-RAY PROPERTIES OF B2 1028+313: A QUASAR AT THE CENTER OF THE ABELL CLUSTER A1030

CRAIG L. SARAZIN

Department of Astronomy, University of Virginia, P.O. Box 3818, Charlottesville, VA 22903-0818; cls7i@virginia.edu,

ANTON M. KOEKEMOER, STEFI A. BAUM, CHRISTOPHER P. O'DEA

Space Telescope Science Institute, 3700 San Martin Drive, Baltimore, MD 21218; sbaum@stsci.edu, koekemoe@stsci.edu, odea@stsci.edu,

FRAZER N. OWEN

National Radio Astronomy Observatory, P.O. Box 0, Socorro, NM 87801; fowen@aoc.nrao.edu,

AND

MICHAEL W. WISE

Center for Space Research, Massachusetts Institute of Technology, Bldg. 37-644, Cambridge, MA 02139; wise@space.mit.edu

*Astrophysical Journal, in press*

### ABSTRACT

X-ray observations with the *ROSATHRI* and with *ASCA* are presented for the nearby radio quasar B2 1028+313, which is located in the cD galaxy at the center of the Abell cluster A1030. We also analyze archival *ROSAT* PSPC observations. We find that the X-ray emission is dominated by the quasar. The flux varied by a factor of about two between the *ROSAT* HRI and *ASCA* observations, which were about one year apart. The X-ray spectrum of the quasar is fit by a single power-law, except at low energies where there is a soft excess. Although the shape of the soft excess is not strongly constrained, it can be fit by a blackbody with a temperature of about 30 eV. There was evidence for extended X-ray emission, which contributed about 25% of the total flux. However, this emission does not appear to be normal X-ray emission from intracluster gas or a central cooling flow. The extended X-ray emission appears to be quite soft; if its spectrum is modeled as thermal emission, the temperature is  $\sim 0.2$  keV, rather than the 5-10 keV expected for ICM emission. The radial surface distribution of the emission was not fit by either the beta model which usually describes ICM emission, or by a cooling flow model. The *ASCA* and *ROSAT* spectra showed no convincing evidence for a thermal component with a cluster-like temperature, either in the overall spectral shape or in emission lines. In addition, the *ROSAT* PSPC image showed that the extended X-ray emission was highly elongated to the NNW and SSE, in the same direction as the extended radio emission from the quasar. We suggest that the extended emission is inverse Compton emission from the extended radio lobes.

*Subject headings:* galaxies: clusters: general — galaxies: clusters: individual (A1030) — galaxies: cD — intergalactic medium — quasars: individual (B2 1028+313) — X-rays: galaxies

### 1. INTRODUCTION

B2 1028+313 is a well-known, nearby ( $z = 0.1782$ ) radio-loud quasar. At radio wavelengths the quasar has a bright, inverted-spectrum core and a one-sided radio jet to the NNW (Gower & Hutchings 1984). On larger scales, the radio emission extends to the NNW and SSE (Owen, White, & Ge 1993; Owen & Ledlow 1997). The radio axis varies with radius around a mean position angle of  $-30^\circ$  (measured from the north to the east). The quasar is a bright X-ray source (Zamorani et al. 1981; Blumenthal, Keel, & Miller 1982; Wilkes & Elvis 1987), whose spectrum shows evidence for a soft X-ray excess above a power-law spectrum (Elvis, Wilkes, & Tannabaum 1985; Wilkes & Elvis 1987; Masnou et al. 1992; Zhou & Yu 1992). The optical spectrum of the quasar is rich in emission lines, and shows a strong rise to the blue (Jackson & Browne 1991; Shastri et al. 1993; Owen, Ledlow, & Keel 1995, 1996). The quasar is also quite bright in the UV (Lanzetta, Turnshek, & Sandoval 1993).

Recently, Owen, Ledlow, & Keel (1995) noticed that the quasar is located in the central cD galaxy of A1030, an Abell richness class 0 cluster (Abell, Corwin, & Olowin 1989). At low redshift, it is uncommon for quasars to be located in the center of a cluster, although higher redshift radio quasars are more strongly clustered (e.g., Yee & Ellingson 1993). The host galaxy of B2 1028+313 is a large, very bright elliptical galaxy

which is similar to other cD galaxies in its optical properties (Ledlow & Owen 1995). The major axis of the galaxy is at a position angle of  $45^\circ$ , which is about  $75^\circ$  away from the radio axis.

The location of this nearby radio quasar in the center of a rich cluster suggests that some portion of the X-ray emission from the system may be coming from intracluster gas. The X-ray luminosity determined from the *Einstein* Observatory data was  $L_X = 7.1 \times 10^{44}$  erg s<sup>-1</sup> (0.3–3.5 keV; Wilkes & Elvis 1987), which is typical for rich Abell clusters. On the other hand, A1030 is a apparently a poor cluster. The X-ray flux is about 30 times higher than would be expected based on the correlation between core X-ray and radio fluxes of core-dominated radio quasars (Worrall et al. 1994). The core in B2 1028+313 provides more than 50% of the 5 GHz radio flux (Gower & Hutchings 1984; Condon et al. 1994), so that B2 1028+313 is core-dominated. On the other hand, its ratio of X-ray to optical flux is more consistent with values for lobe-dominated radio quasars (Worrall et al. 1994), where the X-ray emission may have a large contribution from thermal emission by ambient gas.

The presence of this bright, nearby quasar in the center of a cluster provides an important opportunity to study the interaction between the AGN and its environment. If a portion of the X-ray emission is due to the presence of a hot intracluster medium (ICM), then it is likely that the radio source may in-

interact with this thermal plasma. The radio source associated with the quasar is quite compact (Owen & Ledlow 1997), as might be expected if it were confined by dense ICM. Moreover, the quasar is surrounded by a luminous emission-line region extended on scales  $\sim 25$  kpc (Owen et al. 1998), typical of those found in cooling-flow clusters (e.g., Heckman et al. 1989). Thus, it is possible that the ICM in the region around the quasar is particularly dense, because of a cooling flow.

The location of this quasar in the center of a cluster also provides a light source for searching for absorption by cooler material in the ICM. In this regard, the fact that B2 1028+313 is particularly bright in the UV is very useful. Recently, we used *HST* UV spectra to set very strong limits on the absorbing column of any cooler material in the cluster (Koekemoer et al. 1998). One might also be able to detect cool or hot components of the ICM as absorption lines or edges in the X-ray spectrum of the quasar (Sarazin 1989; Wise & Sarazin 1997).

In this paper, we present *ROSAT* PSPC and HRI images and *ASCA* and *ROSAT* PSPC spectra of the X-ray emission from B2 1028+313 and the surrounding A1030 cluster. The first object of these observations are to determine the X-ray properties of the quasar. Secondly, we want to detect or limit the X-ray emission from intracluster gas in A1030, and to search for evidence for a central cooling flow in this cluster. Third, we want to study the interaction of the radio source with its environment, and search for X-ray emission associated with the extended radio lobes. Finally, if there is evidence for dense ICM around the quasar, we will search for X-ray absorption features in the quasar spectrum due to the ambient gas.

The X-ray observations are presented in § 2. The observed X-ray fluxes are compared and variability detected in § 3. In § 4, we search for extended X-ray emission in the cluster, present X-ray images, and determine the radial surface brightness profile. The X-ray spectra from *ROSAT* and *ASCA* are presented in § 5, and are compared to combinations of nonthermal models for emission by the AGN and thermal models for ICM emission. We also place limits on any emission or absorption lines in § 5.4. The results are discussed in § 6, where we review the X-ray properties of the quasar, and consider the limits on the thermal emission by the ICM. The relationship between the extended X-ray and radio emission is discussed in § 6.3. All distance-dependent values in this paper assume  $H_0 = 50$  km s $^{-1}$  Mpc $^{-1}$  and  $q_0 = 0.5$ . Unless otherwise stated, all of the uncertainties are at the 90% confidence level.

## 2. X-RAY OBSERVATIONS

### 2.1. *ROSAT* HRI Observations

A1030 was observed with the *ROSAT* High Resolution Imager (HRI) during the period 11-27 May, 1996. The total exposure time was 18,600 seconds. In addition to the normal processing of the data, we examined the light curve of a large source-free region to check for any periods of enhanced background, and none were found. Because we are interested in achieving the best possible angular resolution, we also examined the aspect history for any anomalies during the accepted time in the image. None were found. The X-ray image was corrected for particle background, exposure, and vignetting using the SXR software package of Snowden (1995). In addition to A1030/B2 1028+313, 14 other rather weak X-ray sources appear in the HRI image. Only one of these could be identified, and it corresponded to an otherwise unidentified X-ray source from the *Einstein* catalog, 2E 1027.6+3112.

### 2.2. *ROSAT* PSPC Observations

A1030 was also observed with the *ROSAT* Position Sensitive Proportional Counter (PSPC). We have extracted these observations from the public archive to help constrain the spatial extent and spectral properties of the emission from this system. A1030 was observed for 2,481 seconds on 5, February 1992 (RP700433; P.I. B. Wilkes). (Actually, the observation was much longer than this, but most of the data were unusable, apparently because of problems with the aspect solution.) A longer observation of 6,906 seconds was made on the same day with the boron filter in place. The extra opacity of this filter means that the unfiltered and filtered observations produced a similar number of photons from A1030. The PSPC data were screened for periods of high background based on a Master Veto Rate  $> 170$  (Plucinsky et al. 1993), for other times of high background, for periods of 15 seconds after switching to the high voltage, and for periods with an uncertain aspect solution. The resulting live exposure times for the two images were 2,155 seconds for the unfiltered image and 6698 seconds for the image with the boron filter. The average values of the Master Veto Rate were 79.6 for the unfiltered data and 78.6 for the boron filter data.

### 2.3. *ASCA* Observations

A1030 was observed with *ASCA* in two intervals on 1995 May 3-4 and May 7. The two pointings were nearly identical, and have been combined in all of the analysis. Although the data were originally processed with Revision 1 of the standard processing, they were screened using the standard Revision 2 screening criteria. In addition, light curves of the data were constructed and searched for otherwise unrejected data in periods with high background or data dropouts. The total exposures were approximately 36.8 ksec for the SIS and 39.0 ksec for the GIS.

The Solid-state Imaging Spectrometer (SIS) detectors operated with only one chip per detector being active (SOC1 and SIC3). In order to maximize the spectral resolution and the accuracy of the calibration, all of the SIS data were taken in Faint mode and analyzed in Bright2 mode. The SIS data were corrected for the echo effect and dark frame error using FTOOLS FAINT version 3.11. The SIS PI channels were determined using SISPI version 1.1 using the gain file of 110397. Hot and flickering pixels were removed with CLEANSIS version 1.6. A level discriminator (at approximately 0.42 keV) was used to avoid telemetry saturation when SIS data were taken at Medium data rate.

During the period of this observation, the GIS-3 spectral gain was sometimes overestimated by the standard *ASCA* processing (Idesawa et al. 1997). This was corrected using the FTOOLS TEMP2GAIN version 4.1 with the 1996 May 12 version of the gis\_temp2gain calibration file.

## 3. X-RAY FLUXES AND VARIABILITY

In the *ROSAT* HRI observations, a total of  $2763 \pm 61$  counts were detected from A1030, after corrections for background, exposure, and vignetting. This corresponds to a flux of  $4.18 \times 10^{-12}$  ergs s $^{-1}$  in the observed 0.2 – 2.0 keV frame, uncorrected for absorption. We assumed a power-law spectrum

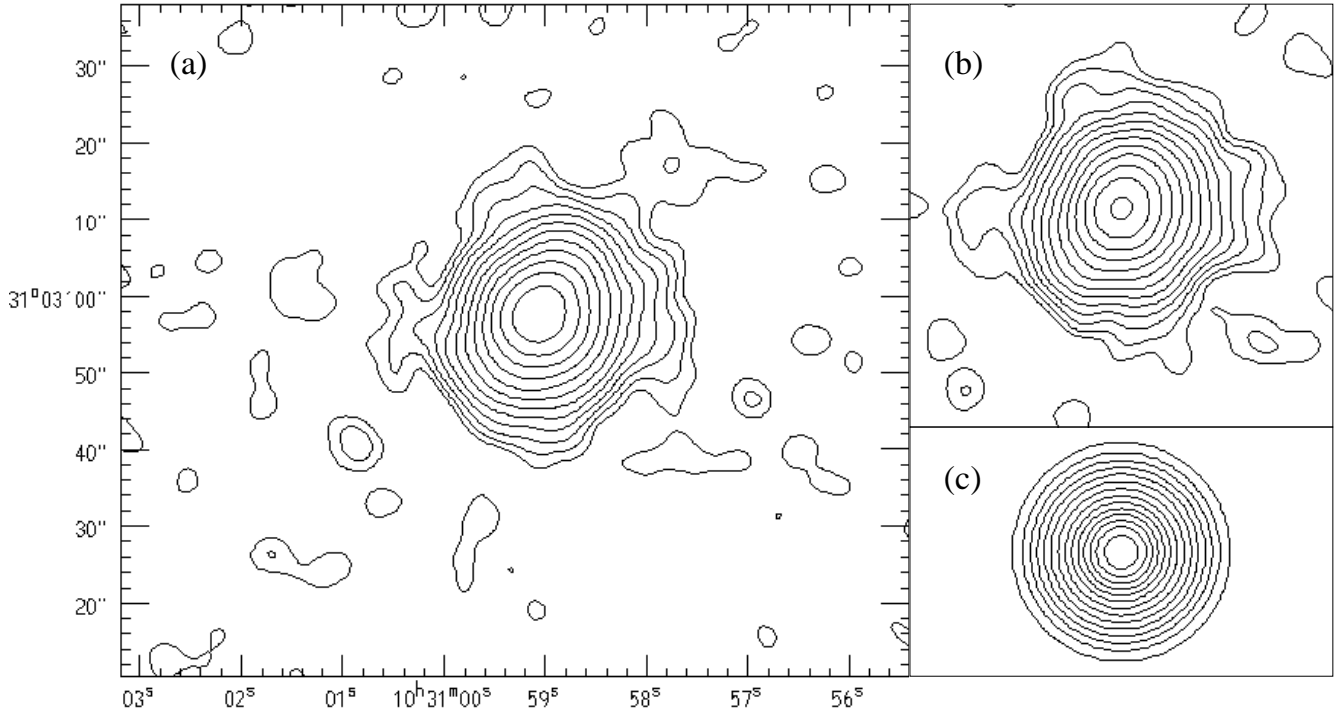


FIG. 1.— (a) Contours of the central *ROSAT* HRI X-ray image of A1030. The image was smoothed with a  $\sigma = 2''$  gaussian. The coordinates are J2000. There are 14 contours logarithmically spaced between 0.02 and 10 counts/pixel (1 pixel =  $0.5'' \times 0.5''$ ). (b) The center of the HRI image of A1030 after “correcting” for the effects of the wobble on the aspect solution, as discussed in the text. The angular scale and contours are the same as in (a). (c) A contour map of the nominal *ROSAT* HRI Point Response Function (PRF). The smoothing, scale, and contours are the same as in (a) and (b).

with a photon index of  $\Gamma = 2.08$  and an absorbing column of  $N_H = 1.21 \times 10^{20} \text{ cm}^{-2}$ .

TABLE 1  
X-RAY FLUX VS. OBSERVATION DATE

Instrument	Observation Date	$f_\nu(1 \text{ keV})$ ( $\mu\text{Jy}$ )
Einstein IPC	1979 May 24	$0.74^{+0.09}_{-0.04}$
ROSAT PSPC	1992 Feb 5	$0.75^{+0.06}_{-0.05}$
ASCA GIS,SIS	1995 May 3–7	$0.43^{+0.02}_{-0.02}$
ROSAT HRI	1996 May 11–27	$0.84^{+0.04}_{-0.03}$

The observed flux for the unfiltered PSPC observation was  $3.80 \times 10^{-12} \text{ ergs s}^{-1}$  (0.2 – 2.0 keV), uncorrected for absorption. The flux in the same band using the boron filtered data was  $4.08 \times 10^{-12} \text{ ergs s}^{-1}$ . These values are within 10% of the HRI flux, measured four years later. The luminosity of A1030 in the rest frame *ROSAT* band 0.2–2 keV is  $L_X = 7 \times 10^{44} \text{ ergs s}^{-1}$ , corrected for absorption.

In order to compare the fluxes measured at different epochs using different instruments, we also determined the observed flux density  $f_\nu$  at 1 keV, uncorrected for absorption. We adopted this energy because it was within the band pass of *ROSAT*, *Einstein*, and *ASCA*, and this value was derived by Wilkes & Elvis (1987) from the *Einstein* IPC observation. In Table 1, the flux densities measured by the different instruments at different times are given in  $\mu\text{Jy}$  ( $1 \mu\text{Jy} \equiv 10^{-29} \text{ ergs}$

$\text{cm}^{-2} \text{ s}^{-1} \text{ Hz}^{-1}$ ). The uncertainties are at the 90% confidence level for a single interesting parameter. Only statistical uncertainties are included; the calibration errors are probably at least as large as the statistical uncertainties in most cases. The second column gives the dates of the observations. The *ROSAT* PSPC and HRI fluxes assume the best-fit single power-law fit to the *ROSAT* PSPC X-ray spectrum (§ 5.1). Also, the flux listed was derived from the unfiltered PSPC observation. The observation with the boron filter, which occurred on the same date as the unfiltered observation, gave a flux which was 7% higher (§ 5.1). This is within the uncertainties in the fluxes; it is also likely that the calibration errors in the two instruments are of this order. The *ASCA* flux is based on the SIS0, GIS2, and GIS3 instruments. The flux in SIS1 was slightly lower (§ 5.2), but consistent within the likely calibration uncertainties.

The fluxes from the *Einstein* and *ROSAT* PSPC are remarkably consistent, given the passage of 13 years. The flux from the *ROSAT* HRI is only slightly higher, and marginally consistent within the uncertainties. On the other hand, the observed flux during the *ASCA* observation was about a factor of two lower than any of the other fluxes. This result does not depend on the particular spectral model used to convert count rates into fluxes for each of the instruments. Thus, we conclude that although the X-ray flux may have remained approximately constant for much of the time since 1979, it must on occasion vary by at least a factor of two on time scale as short as a year. On the other hand, there was no significant evidence for any variation during the period of *ROSAT* HRI observation, during the *ROSAT* PSPC observation, or during the *ASCA* observation. This may

indicate that the source doesn't vary by a large factor on time scales as short as a few days to two weeks.

The variability of the source on time scales of a year means that at least 50% of the X-ray emission is from the quasar rather than the cluster.

#### 4. SPATIAL STRUCTURE

##### 4.1. *ROSAT* HRI Spatial Distribution

Figure 1a shows the contour map of the inner approximately  $100'' \times 90''$  of the HRI image of A1030. The image was smoothed with a gaussian kernel with  $\sigma = 2''$ , and the 14 contours are logarithmically spaced between 0.02 and 10 counts/pixel (1 pixel =  $0.5'' \times 0.5''$ ). The centroid of the X-ray emission was at R.A. =  $10^{\text{h}}30^{\text{m}}59^{\text{s}}.1$  and Dec. =  $31^{\circ}02'58''$  (J2000), which is within  $3''$  of the position of the quasar B2 1028+313. For comparison, Figure 1c shows a contour map of the nominal *ROSAT* HRI Point Response Function (PRF) on the axis of the instrument (David et al. 1993), smoothed in the same way as the data. The image of A1030 appears somewhat more extended than that expected from a point source, and is elongated at a position angle (*PA*) of about  $-29^{\circ}$  (measured counterclockwise from north). None of the other sources in the HRI image are bright enough to usefully test for a similar extension in the image.

The HRI observation of A1030 was done in 6 OBIs (observational intervals) during the period 11-27 May, 1996. The image in Figure 1a resulted from combining all of these observations. To check for possible offsets in the aspect solution between these OBIs, we produced images from each of the separate OBIs. They all gave a consistent centroid for the X-ray emission, and all showed an elongation in the same general direction ( $PA \approx -29^{\circ}$ ).

During most pointed observations with *ROSAT*, the satellite is "wobbled" by several arcmin with a period of several hundred seconds. Morse (1994) has suggested that errors in the aspect solution during wobbling can result in extended and elongated images of point sources. Although he argues that the aspect errors are associated with the wobble, Morse finds that the observed elongations of the images of point sources aren't necessarily parallel to the projection of the wobble on the sky. The Nominal Roll Angle for the observation of A1030 was  $-14.98^{\circ}$  (measured clockwise from north). This implies that the projection of the wobble on the sky was at  $PA \approx -30^{\circ}$ . Unfortunately, this is very close to the observed direction of elongation of the central part of the image of A1030 in Figure 1a. This increases the concern that extent and elongation of our HRI image of A1030 might be due to the effects of the wobble, rather than due to extended emission from the cluster.

Morse (1994) developed a technique to attempt to correct for aspect errors due to the wobble. Unfortunately, his original technique can only be applied to very bright sources. In Appendix A, we present a variant on Morse's algorithm which can be applied to fainter sources. The resulting image of the center of A1030 is shown in Figure 1b. The center part of this image is considerably narrower than the original image (Fig. 1a). However, beyond a few arcsec, the "wobble-corrected" image is very similar to the original image, and is elongated in nearly the same direction ( $PA = 23^{\circ}$ ). The wobble-corrected image still appears somewhat more elongated than the HRI PRF (Fig. 1c). We conclude that the wobble-corrected image in Figure 1b actually is a better representation of the correct image of the central region of A1030. However, the restriction to a finite set of

regions on the detector implies that this image is missing flux at larger distances from the center of the A1030, and we use the original image beyond the central  $10''$ , and for determining the total flux from the source.

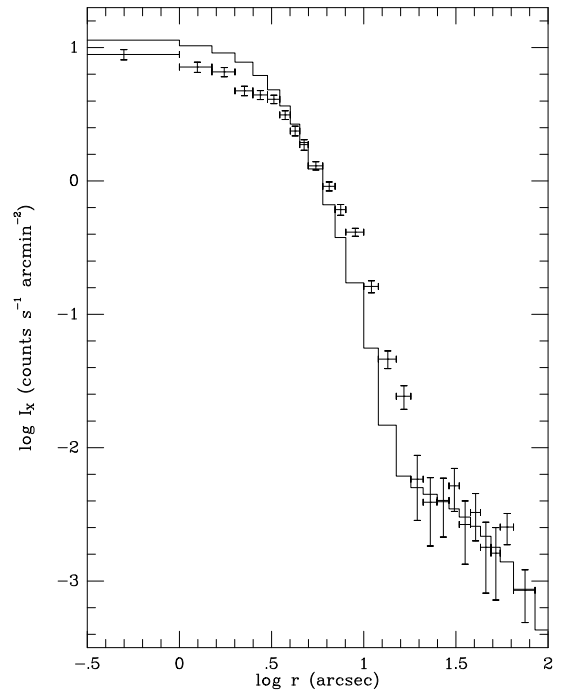


FIG. 2.— The *ROSAT* HRI surface brightness of A1030 as a function of the radius, corrected for background, exposure, and vignetting. The data points give the surface brightness measured in circular annuli with  $1-\sigma$  uncertainties. The solid histogram is the HRI Point Response Function (PRF), normalized to the data and accumulated in the same annuli as the data.

To determine or limit the flux from A1030 which is due to extended cluster emission, we accumulated the HRI counts in annuli centered on the X-ray centroid. All of the annuli had at least 20 counts to assure the applicability of Gaussian statistics. Other X-ray sources were excluded. The resulting surface brightness profile for the wobble-corrected image is shown in Figure 2. The data points give the observed surface brightness, corrected for background, exposure, and vignetting. For comparison, we constructed an image of the *ROSAT* PRF, and normalized it to have the same number of counts within a radius of  $100''$  as the actual image. Note that the broad wings on the image ( $r \gtrsim 15''$ ) are apparently just due to the PRF; this is the "halo" produced by the electrostatic screen on the HRI. This halo severely limits our ability to detect extended faint emission with the HRI. However, in the central regions, even the wobble-corrected image is broader than the PRF. This broadening is most evident at radii of  $r \approx 10'' \approx 40$  kpc. The best-fit point source model for the image has  $\chi^2 = 264.6$  for 25 degrees of freedom (d.o.f.).

We tried a number of simple models to fit the HRI surface brightness. Some of the results are shown in Table 2, which also gives the results of fits to the PSPC surface brightness (§ 4.1). All of the models include a point source at the center. The model surface brightness was convolved with the PRF of the instrument, and accumulated in the same annuli used for the data. The best fit model was determined by minimizing  $\chi^2$ . The quoted uncertainties are 90% confidence regions for a single interesting parameter ( $\Delta\chi^2 = 2.706$ ). For each model,

TABLE 2  
Fits to the ROSAT X-Ray Surface Brightness

Detector	Model	$r_X$ (arcsec)	$\beta$	$\gamma$	Extended Fraction (%)	$\chi^2/\text{d.o.f.}$
HRI	Point Source				(0)	264.6/25 = 10.58
HRI	Gaussian	$5.2 \pm 0.5$			$57^{+6}_{-5}$	25.2/23 = 1.09
HRI	Beta Model	$31^{+4}_{-20}$	>2.02	(0)	$42^{+3}_{-3}$	22.6/22 = 1.03
HRI	Cooling Flow	$31^{+5}_{-20}$	>2.02	<0.91	$42^{+6}_{-5}$	22.6/21 = 1.08
PSPC	Point Source				(0)	218.4/25 = 8.74
PSPC	Gaussian	$32 \pm 4$			$35^{+2}_{-2}$	25.2/23 = 1.09
PSPC	Beta Model	$55^{+143}_{-26}$	>0.95		$29^{+3}_{-2}$	18.5/22 = 0.84
PSPC	Cooling Flow	$55^{+219}_{-26}$	>0.95	<1.41	$29^{+7}_{-5}$	18.5/21 = 0.88

the Table gives a spatial scale parameter  $r_X$ , and the fraction of the flux within  $2'$  radius in the extended component. The best-fit value of  $\chi^2$  and the number of degrees of freedom are also given. Parameters in parentheses are fixed by assumption.

In general, we found that a large number of models could fit the extended component of the HRI surface brightness, because it is only seen clearly over a small range of radii. Each of these fits required a point source as well as an extended component. For example, Table 2 shows the results of fitting a Gaussian surface brightness component (where  $r_X = \sigma$  for the Gaussian). We also fit the standard isothermal beta model,

$$I_X(r) = I_o \left[ 1 + \left( \frac{r}{r_X} \right)^2 \right]^{-3\beta+1/2}. \quad (1)$$

For the isothermal beta model, the value of  $\beta$  is also given. In the beta model, the value of  $\beta$  is not very well constrained, but the lower limit of 2.02 is much larger than the value found for typical clusters ( $\sim 0.6$ ). This implies that the X-ray surface brightness of the extended component in A1030 falls off much faster at large radii than would be expected for cluster emission. Note that the value of the core radius  $r_X \approx 31'' \approx 120$  kpc, which is a reasonable value for the core radius of a cD cluster.

We also tried a model which provides a reasonable fit to the X-ray surface brightness profiles of many nearby clusters with cooling flows. It has the same form as the beta model at large radii, but the surface brightness increases as a power-law function of the radius at small radii:

$$I_X(r) = I_o \left( \frac{r}{r_X} \right)^{-\gamma} \left[ 1 + \left( \frac{r}{r_X} \right)^2 \right]^{-3\beta+1/2}. \quad (2)$$

For nearby cooling flow clusters,  $\gamma \approx 1$  (e.g., Fabian 1994). The spatial scale  $r_X$  in this model is more closely related to the cooling radius in the cluster than to the core radius. The resulting of fitting this model to the HRI observations are shown in Table 2. The best-fit value of  $\gamma$  is 0.03, which is quite small. This makes the cooling flow model nearly identical to the beta model. Thus, there is no strong evidence for a cooling flow from the ROSAT HRI image.

#### 4.2. ROSAT PSPC Spatial Distribution

We also studied the spatial extent of the X-ray emission in A1030 using the ROSAT PSPC data. Although we initially attempted to determine the image and surface brightness profile separately for the unfiltered and boron filter data, and to use only the hard band (0.52–2.0 keV) data, there were too few counts. Thus, we broadened the photon energy band used ( $11 \leq PI \leq 235$ ), and merged the unfiltered and boron filter data. Figure 3 shows X-ray contours of the merged ROSAT PSPC image the central region of A1030. The image has been corrected for background and vignetting, but not exposure as it is the sum of the unfiltered and boron filter image with different exposures and responses. The image was smoothed with a gaussian kernel with  $\sigma = 8''$ . For comparison, the lower right panel shows the ROSAT PSPC PRF for these data, after the same smoothing as the data. The PRF of the PSPC is energy dependent. To determine the correct PRF to apply to these data, we determined the distribution of counts within  $2'$  radius of the center as a function of the photon energy channel ( $PI$ ). Then we constructed a number of PRFs for different photon energies, and weighted them by the observed fraction of counts in the relevant range of  $PI$  values.

The observed image of A1030 is wider than the PRF at radii  $\gtrsim 25''$ . While the morphology of the extension at small radii is unclear from the PSPC image, at radii beyond  $\sim 1'$  the X-ray emission is strongly elongated to the NNW and SSE at a position angle of about  $-30^\circ$ . This is similar to the direction of elongation of the HRI image (Figure 1). In addition to the elongation, two compact X-ray sources are located at nearly equal distances of about  $3/5$  from the nucleus of B2 1028+313 along approximately the same position angle as the X-ray elongation (at  $10^h30^m51^s$ ,  $31^\circ06'$ , and  $10^h31^m06^s$ ,  $31^\circ00'$ ). These sources also appear in the ROSAT HRI image. It is unclear whether they are extended or point sources, or whether they are related to B2 1028+313 or not.

The extended X-ray emission in Figure 3 is very soft. Although there are too few photons to extract a spectrum, we determined X-ray colors for the inner  $1'$  circle and  $1'-3'$  annulus about the center. First, we determined an X-ray color from the ratio of the counts in the Snowden (1995) R4-R7 bands (approximately 0.52–2.02 keV) to those in the Snowden R1L-R2 bands (approximately 0.11–0.41 keV) in the unfiltered PSPC image. In the inner  $1'$ , this ratio is  $0.91 \pm 0.10$ . There is no significant detection of hard photons in the  $1'-3'$  annulus, and the upper limit of the color is  $<0.29$  at the 90% confidence level.

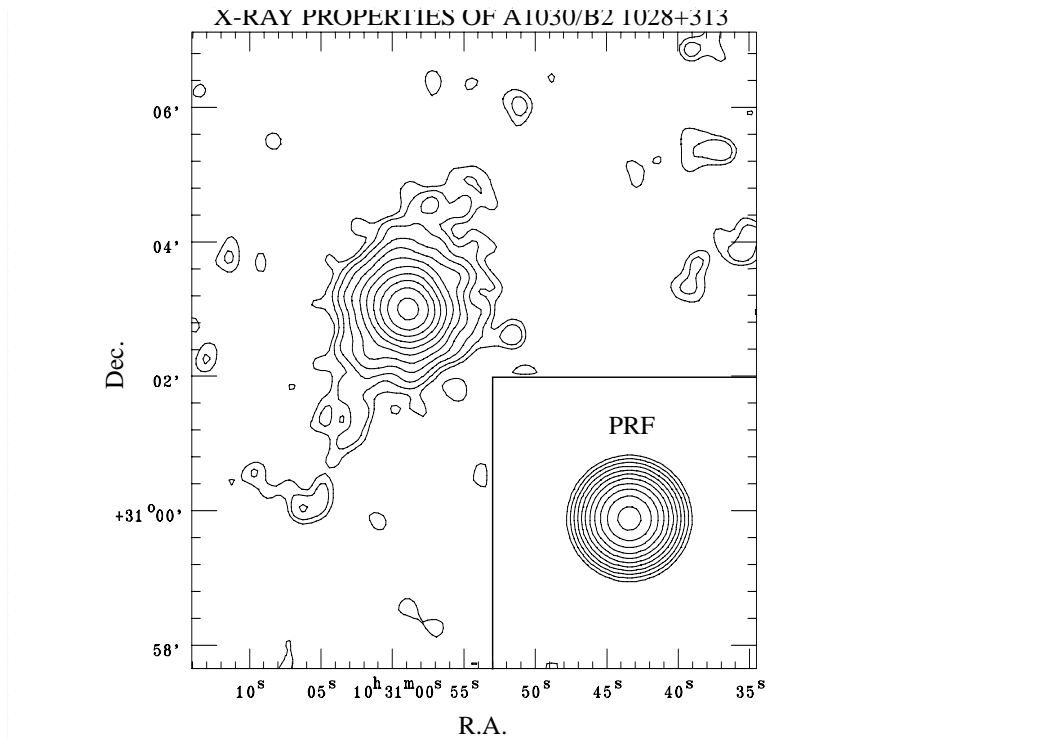


FIG. 3.— Contours of the central *ROSAT* PSPC X-ray image of A1030. The image is based on the sum of the unfiltered and boron filter data. The image has been corrected for background and vignetting, but not for exposure. The image was smoothed with a  $\sigma = 8''$  gaussian. The coordinates are J2000. There are 11 contours logarithmically spaced between 0.05 and 20 counts/pixel (1 pixel =  $4'' \times 4''$ ). The panel in the lower right corner gives the *ROSAT* PSPC PRF for this image, smoothed and contoured in the same way as the data.

This radial variation in the color is too large to be due to the energy dependent PRF of the *ROSAT* PSPC. Second, we determine a X-ray color from the ratio of the boron filtered PSPC count rate to that for the unfiltered PSPC image for the  $1'-3'$  annulus. This gave a ratio of  $0.21 \pm 0.09$ . Both of these values of the X-ray color are quite soft. If the emission were thermal from diffuse gas with a heavy element abundance of 0.3 of solar and subject to Galactic absorption, the temperature of the gas would be  $kT \approx 0.20$  keV. Alternatively, if it is due to a power-law component with Galactic absorption, the photon index of the power law is  $\Gamma = 2.9 \pm 0.4$ . With this spectrum, the count rates imply a total flux density at 0.2 keV of about  $0.7 \mu\text{Jy}$  in the  $1'-3'$  annulus. If we adopt the same power-law index as observed for the radio emission from the same region ( $\alpha = 1.45$ ,  $\Gamma = 2.45$ , § 6.3), then the flux at 0.2 keV is about  $0.5 \mu\text{Jy}$ .

We also determined the radial surface brightness profile of A1030 from the PSPC data. Counts were accumulated in annuli centered on the X-ray centroid. The observed surface brightness was corrected for background, exposure, and vignetting. Other X-ray sources were excluded. We separately extracted the surface brightness profiles for the unfiltered and boron filter data, and corrected them for background, relative exposure, and vignetting. The two profiles agreed to within the uncertainties. Then, we added the two profiles together to improve the signal-to-noise ratio. All of the annuli had at least 20 counts to assure the applicability of Gaussian statistics. The resulting merged PSPC surface brightness profile is shown in Figure 4. Note that we have not normalized the surface brightness to the total exposure, as this is not really meaningful for the sum of the unfiltered and boron filtered data.

The instrument PRF discussed above was normalized to have the same number of counts within a radius of  $2'$  as the actual im-

age, and was accumulated in the same annuli as the data. The resulting PRF surface brightness is shown as a solid histogram in Figure 4. The best-fit point source model for the surface brightness has  $\chi^2 = 218.4$  for 25 d.o.f.

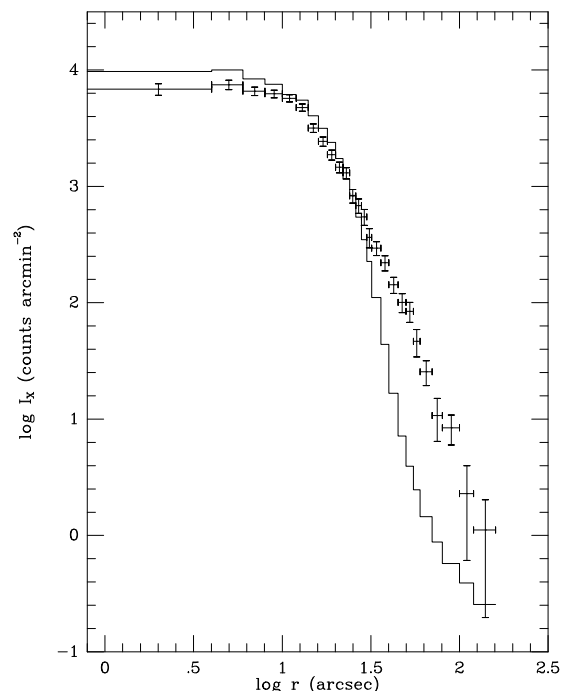


FIG. 4.— The *ROSAT* PSPC surface brightness of A1030 as a function of the radius, corrected for background, exposure, and vignetting. The data points

give the surface brightness measured in circular annuli with  $1\text{-}\sigma$  uncertainties. The data are the sum of the surface brightness in the unfiltered and boron filtered data. The solid histogram is the PSPC Point Response Function (PRF), normalized to the data and accumulated in the same annuli as the data.

We also included an extended component in the fits, which was modeled using a Gaussian, the beta model (eq. 1), or the cooling flow model (eq. 2). The results are shown in Table 2. The beta model provided an acceptable fit, but the value of  $\beta$  was larger than found for typical nearby clusters. The addition of a cooling flow at the center did not improve the fit significantly.

Given that the extended X-ray emission in the PSPC image is highly elongated, has a very soft spectrum, and does not follow the surface brightness profile expected for the ICM, it seems unlikely that the X-rays in the elongated features in Figure 3 are due to normal intracluster gas. To limit the X-ray contribution from normal ICM, we determined the X-ray emission in Figure 3 in an annulus between  $1'$  and  $3'$ , but excluding wedges which contained the X-ray extensions to the NNW and SSE. Only  $49 \pm 20$  counts were detected above the background in this region, of which  $7 \pm 6$  were expected from spill over of the PRF from the central source. Thus, the net count was  $42 \pm 21$ . For comparison, the total count above background within  $3'$  was  $2276 \pm 81$ . Correcting for the area of the X-ray elongation which were excluded from this determination, we find that any circularly symmetric ICM emission at projected radii beyond  $1'$  accounts for  $<4\%$  of the X-ray emission in the *ROSAT* PSPC band.

## 5. X-RAY SPECTRA

### 5.1. *ROSAT* PSPC Spectra

The PSPC spectra from the unfiltered and boron filter observations were extracted from a circle of  $2'$  radius from the center of A1030. The spectra were corrected for background. The photon energy channels below 0.2 keV and above 2.2 keV were discarded, and the spectra were grouped so that each spectral bin had at least 20 counts. The spectra were fit using the XSPEC program. Initially, the Galactic absorbing column was fixed at  $N_H = 1.98 \times 10^{20} \text{ cm}^{-2}$ . Based on NRAO Greenbank 140 ft. observations towards this target, this should be a reasonably accurate value (Elvis, Lockman, & Wilkes 1989). We fit the emission from the source as a power law, with the number of emitted photons per unit photon energy  $E$  varying as  $E^{-\Gamma}$ . The unfiltered and boron filter data were initially fit separately; the results are shown in rows 1 and 2 of Table 3. The two fits gave values of the photon spectral index  $\Gamma$  in reasonably agreement. The boron filter data suggested a slightly higher normalization (by about 5%) than the unfiltered data. This difference would seem to be within the range of calibration uncertainties.

We then fit the two PSPC spectra jointly to a single power-law, while allowing the normalization of the spectra to differ slightly. The result is shown in row 3 of Table 3. Again, this is a reasonably good fit. These fits to the spectra are shown in Figures 5 and 6.

There is some evidence for a soft X-ray excess in the data from both of the instruments. A similar result was found by Wilkes & Elvis (1987) based on the *Einstein* IPC spectrum of this object. As one method of fitting this soft excess, we allowed the Galactic absorbing column to vary. This significantly improved the fit to the PSPC spectra (row 4 of Table 3). For comparison, Wilkes & Elvis (1987) found that the

*Einstein* IPC spectrum was fit by a power-law with  $\Gamma = 1.5^{+0.3}_{-0.1}$  and  $N_H \leq 1.3 \times 10^{20} \text{ cm}^{-2}$ . The *ROSAT* PSPC spectral index is somewhat larger than the *Einstein* value, but this may reflect the inadequacy of modeling the soft X-ray as reduced X-ray absorption, and the wider energy band pass of *Einstein*.

It is more physically plausible to model the soft X-ray excess as an additional emission component. None of the spectra presented in this paper strongly constrain the shape of this component. As a result, we have chosen arbitrarily to model the soft X-ray excess as a blackbody. Row 5 in Table 3 shows the result of a fit, fixing the absorbing column at the Galactic value, but adding a soft blackbody component. The temperature is not very strongly constrained. This excess soft X-ray component provides about 9% of the total 0.2–10 keV X-ray luminosity of the quasar (the fraction listed in Table 3).

We also tried to fit the PSPC spectrum using a single temperature thermal MEKAL model for emission by the intracluster medium. A purely thermal model for the PSPC X-ray spectrum did not provide an acceptable fit, and required very low temperatures and abundances for the intracluster gas (row 6 of Table 3), which are not consistent with the values found in other clusters.

### 5.2. *ASCA* Spectra

The GIS and SIS spectra of the source were extracted using a circular regions with radii of  $6'$  and  $4'$ , respectively. GIS background spectra were extracted using the same regions of the detectors from the 1994 May blank sky calibration fields. The GIS background data were cleaned in the same way as the source data. The histogram of the values of the Cut Off Rigidity (*COR*) during the observation was determined, and the blank sky background field observations were summed so as to reproduce the *COR* distribution of the A1030 observation for both GIS2 and GIS3. We also tried using backgrounds accumulated from symmetric positions on the detectors during our own observation. These gave consistent results, although the statistic uncertainties were much smaller for the blank sky backgrounds.

Determining an appropriate background spectrum for the SIS observations proved to be more difficult. We tried accumulating local backgrounds from our own observation. However, in 1-CCD mode, there is very little area left over on the chip once the source region is excluded. Moreover, the background spectrum is then accumulated from a less sensitive region of the detector than the source spectrum. The blank sky SIS observations in the calibration database were all taken in 4-CCD bright mode, and so have a somewhat different response than the data in our observation. Also, the calibration observations were done early in the mission, and the SIS detectors have degraded significantly since then. We found that these observations gave background spectra which were inconsistent with our observations. Instead, we used a blank sky observation done at about the same time as our observation and extracted from the archive (observation 73016000). This high Galactic latitude observation was done in 1-CCD faint mode, but without the use of the level discriminator. The background spectra were accumulated from the same regions of the detectors as our source spectra.

The GIS and SIS spectra were limited to the photon energy ranges of 0.55–11 keV and 0.45–11 keV, respectively. The spectra were binned so that each channel contained at least 20 counts, so that  $\chi^2$  statistics could be applied. The two GIS instruments were found to give consistent spectral fits, both in terms of the shape of the spectra and the normalization. The

TABLE 3  
 ASCA and ROSAT X-Ray Spectral Fits

Row	Instrument	$N_H$ ( $10^{20} \text{ cm}^{-2}$ )	Power Law $\Gamma$	Blackbody or Thermal Model			$\chi^2/\text{d.o.f.}$
				$kT$ (keV)	Abund. (solar)	Fraction (%)	
1	PSPC Unfilt.	(1.98)	$2.32^{+0.08}_{-0.09}$			(0)	41.3/36 = 1.15
2	PSPC Boron	(1.98)	$2.47^{+0.13}_{-0.15}$			(0)	41.2/42 = 0.98
3	PSPC	(1.98)	$2.35^{+0.08}_{-0.07}$			(0)	84.7/79 = 1.07
4	PSPC	$1.21^{+0.41}_{-0.37}$	$2.08 \pm 0.17$			(0)	75.9/78 = 0.97
5	PSPC	(1.98)	$2.16 \pm 0.15$	$0.022^{+0.013}_{-0.015}$	BB	$9^{+1}_{-4}$	74.8/77 = 0.97
6	PSPC	(1.98)		0.82	0.0	(100)	165.8/78 = 2.13
7	ASCA GIS	(1.98)	$1.71 \pm 0.06$			(0)	231.2/245 = 0.94
8	ASCA GIS	<5.91	$1.70 \pm 0.07$			(0)	231.1/244 = 0.95
9	ASCA SIS	(1.98)	$1.84 \pm 0.04$			(0)	258.5/287 = 0.90
10	ASCA SIS	$5.62^{+2.45}_{-2.35}$	$1.95 \pm 0.08$			(0)	252.0/286 = 0.88
11	ASCA	(1.98)	$1.80 \pm 0.03$			(0)	498.9/534 = 0.93
12	ASCA	$2.71^{+1.99}_{-1.92}$	$1.82 \pm 0.06$			(0)	498.5/533 = 0.94
13	ASCA	(1.98)		$5.34^{+0.40}_{-0.38}$	$0.22^{+0.11}_{-0.11}$	(100)	562.4/533 = 1.06
14	ASCA	(1.98)	$1.80^{+0.06}_{-0.04}$	(7)	(0.3)	<21	498.9/533 = 0.94
15	ASCA & PSPC	(1.98)	$1.88 \pm 0.03$			(0)	693.0/614 = 1.13
16	ASCA & PSPC	$0.61^{+0.16}_{-0.15}$	$1.78 \pm 0.03$			(0)	587.4/613 = 0.96
17	ASCA & PSPC	(1.98)	$1.81 \pm 0.03$	$0.028^{+0.012}_{-0.055}$	BB	$15 \pm 1$	586.9/612 = 0.96
18	ASCA & PSPC	$0.56^{+0.15}_{-0.15}$	$1.80^{+0.12}_{-0.05}$	(7)	(0.3)	<21	589.2/614 = 0.96

normalization of the SIS0 spectrum was also consistent with that of the two GIS detectors. However, while the two SIS instruments gave consistent fits for the shape of the spectrum, the SIS1 spectra give slightly lower fluxes (by about 5%). Thus, the normalization of the SIS1 instrument was allowed to vary relative to the others. All of the spectral fitting was done with separate response matrixes for all four *ASCA* instruments. However, for the purpose of plotting the spectra and models, we created total GIS and SIS spectra, averaging over the responses of each of the two detectors. Also, in the plots of the overall spectra, we summed up to five adjacent channels to make the plots less confusing.

The best-fit power-law spectral fit to the GIS2 and GIS3 spectra assuming the measured Galactic column are shown in row 7 of Table 3. A power-law is a reasonably good fit to the GIS spectra, although the slope is considerably flatter than that required to fit the PSPC spectra. The total GIS spectrum and best-fit model are shown in Figure 7. The GIS has too little soft X-ray sensitivity to strongly constrain the absorbing column; if the absorption is allowed to vary, only an upper limit is found (row 8 of Table 3).

A power-law spectrum also was a good fit to the SIS data. The best-fit model assuming the Galactic column is shown in row 9 of Table 3 and Figure 8. The power-law slope is intermediate between that derived from the GIS and that from the PSPC. The observed spectrum is below the model in the region of the oxygen K-edge; when the absorption is allowed to vary, the best-fit absorption value is considerably above the Galactic value (row 10 of Table 3).

We also fit a power-law model jointly to the *ASCA* GIS and SIS spectra. The results for Galactic or variable absorption are shown in rows 11 and 12 of Table 3. A single power-law spec-

trum with Galactic absorption provided an acceptable fit to the SIS and GIS spectra; allowing the absorption to vary did not improve the fit significantly. The best-fit joint spectrum is somewhat inconsistent with the individual SIS and GIS spectral fits; for Galactic absorption, these gave  $\chi^2 = 489.7$  for 532 d.o.f. This difference is statistically significant; however, the difference could also be explained by a small ( $\sim 3\%$ ) systematic error in the responses of the GIS and/or SIS.

A purely thermal model for the *ASCA* spectrum provided an adequate fit (row 13 of Table 3). Unlike the thermal fit to the PSPC spectrum (row 6 of Table 3), the temperature and abundance were not unreasonable. However, this is a much poorer fit than the power-law model. We also tried fitting the *ASCA* spectra assuming both a power-law and thermal contribution. The best-fit thermal contribution was zero. Obviously, the parameters of the thermal model could not be determined, so we assumed  $kT = 7$  keV and an abundance of 0.3 of solar. As shown in row 14 of Table 3, the maximum thermal contribution to the spectrum was 21% of the 0.2–10 keV rest frame X-ray luminosity, or  $L_X(\text{thermal}) < 1.6 \times 10^{44} \text{ ergs s}^{-1}$ .

### 5.3. Joint Fits to ROSAT and ASCA Spectra

We also tried to fit simultaneously the *ROSAT* PSPC unfiltered and boron filter spectra along with the *ASCA* SIS and GIS spectra. Of course, between the *ROSAT* PSPC observation and the *ASCA* observation, the flux from the source dropped by a factor of nearly two (Table 1). Thus, we are assuming that the shape of the spectrum remained unchanged while the flux varied, which may very well be wrong. Obviously, we have to allow the normalization of the spectrum to differ between the *ROSAT* PSPC and *ASCA* spectra. Row 15 in Table 3 shows



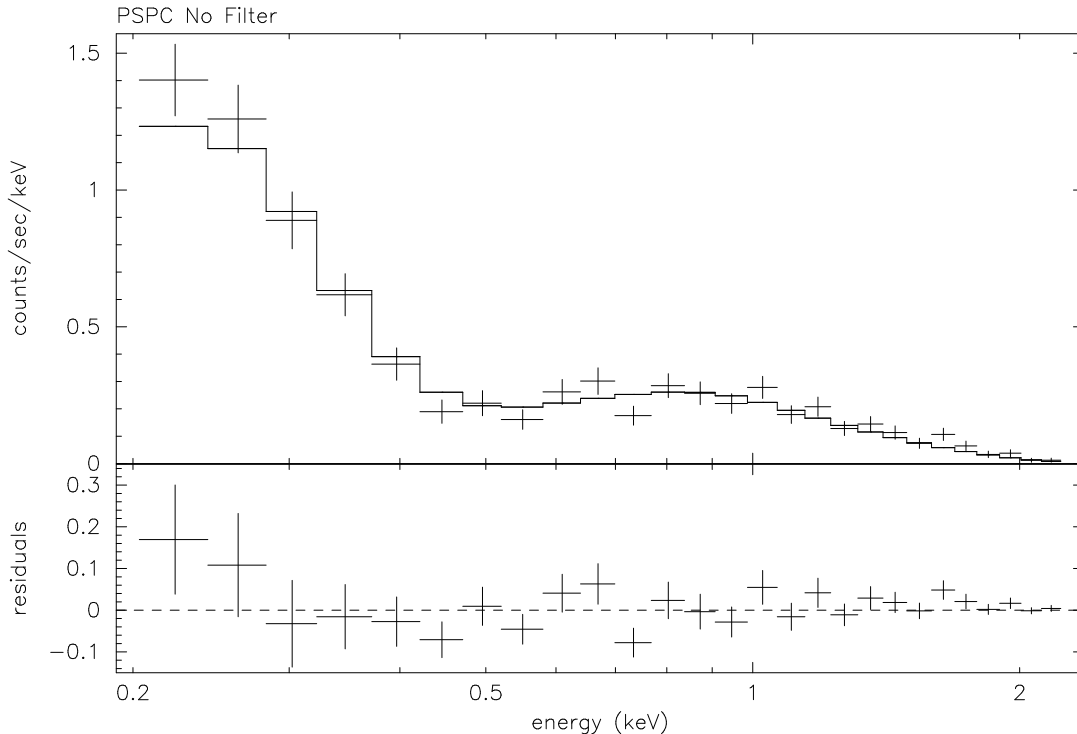


FIG. 5.— The *ROSAT* X-ray spectrum of A1030 for the unfiltered data. The upper panel gives the data and the best-fit power-law model for the unfiltered and boron filter data (row 3 of Table 3) assuming the measured Galactic absorption of  $N_H = 1.98 \times 10^{20} \text{ cm}^{-2}$ . The crosses give the data points with  $1\text{-}\sigma$  uncertainties bars, while the histogram is the model. The width of the data points or histogram steps is the width of the energy channels used to accumulate the data. The lower panel gives the residuals to the fit (in counts/sec/keV).

the best joint spectra fit, assuming a power-law spectrum and the Galactic absorbing column. This is not a terrible fit, but it is much worse than the separate fits to the *ROSAT* PSPC and *ASCA* spectra. This may indicate that the spectrum varied somewhat between this two epochs.

Alternatively, the *ROSAT* PSPC spectra suggested the presence of an excess soft X-ray component. If we model this by allowing the absorbing column to vary, the joint *ASCA* and PSPC spectral fit is considerably improved (row 16 of Table 3). It is not quite as good a fit as the fits to the individual spectra, and the difference is statistically significant. On the other hand, the difference could also be accounted for by a small systematic error of  $\sim 3\%$  in the responses of the instruments. If we model the soft X-ray excess as a blackbody, the spectral parameters are shown in row 17 of Table 3. The temperature of the blackbody is poorly determined but is about 30 eV. This soft component provides about 15% of the 0.2–10 keV luminosity of the quasar.

In order to provide another limit on the X-ray contribution of intracluster gas, we fit the joint *ROSAT* PSPC and *ASCA* spectra to a model with both a power-law component and a thermal component. Since the X-ray emission of the intracluster gas cannot vary on observable time scales, we required that the normalization of the thermal component be constant. It would also be difficult to understand how the absorbing column toward the intracluster gas could be lower than the Galactic value, so we fixed this quantity as well. The best-fit spectral model had only a small thermal contribution, and the spectral properties of this component were not well-determined. For the purposes of limiting the thermal contribution, we fixed the gas temper-

ature at  $kT = 7$  keV and the abundances at 0.3 of solar. The results are shown in row 18 of Table 3. The absorbing column value applies to the power-law component. The upper limit on the contribution of the intracluster gas is 21% of the 0.2–10 keV rest frame X-ray luminosity during the *ROSAT* PSPC observation (the value in Table 3), or 36% of the *ASCA* luminosity. The upper limit on the intracluster gas luminosity is  $L_X(\text{thermal}) < 2.6 \times 10^{44} \text{ ergs s}^{-1}$  (0.2–10 keV).

We also tried modeling the cluster emission assuming a cooling flow spectrum. The upper limits here are even tighter:  $< 8\%$  of the *ROSAT* flux or  $< 14\%$  of the *ASCA* flux, corresponding to limits on the luminosity of  $L_X(\text{thermal}) < 0.9 \times 10^{44} \text{ ergs s}^{-1}$  (0.5–10 keV) or limits on the cooling rate of  $\dot{M} < 93 M_\odot \text{ yr}^{-1}$ .

TABLE 4  
ASCA LIMITS ON EMISSION AND ABSORPTION LINES

Line	Redshifted Line Energy (keV)	Equivalent Width Limits (eV)	
		Emission	Absorption
Fe XXVI $1s\text{-}2p$	5.91	41	111
Fe XXV $1s^2\text{-}1s2p$	5.67	44	106
S XVI $1s\text{-}2p$	2.23	43	79
S XV $1s^2\text{-}1s2p$	2.09	95	68
Si XIV $1s\text{-}2p$	1.70	125	79
Si XIII $1s^2\text{-}1s2p$	1.58	33	54

#### 5.4. Limits on Emission or Absorption Lines

In addition to its overall effect on the shape of the X-ray spectrum, any thermal intracluster gas component would produce X-ray line emission. We have searched for evidence of

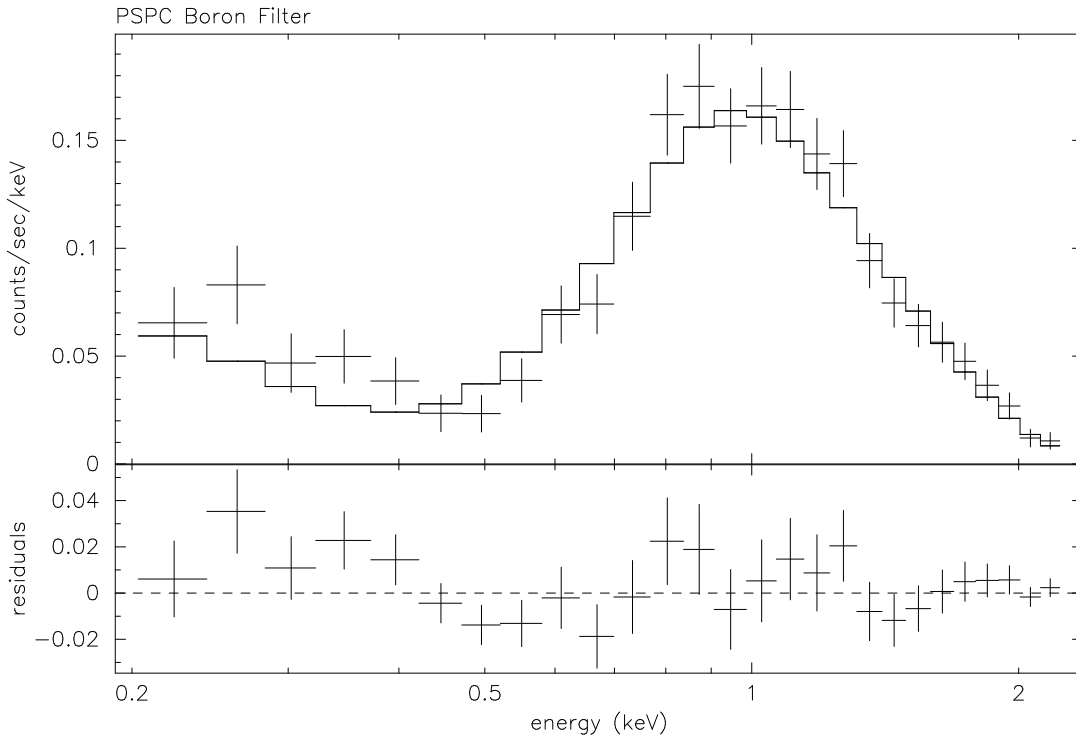


FIG. 6.— The *ROSAT* X-ray spectrum of A1030 for the boron filter data. The notation and model are the same as in Figure 5.

line emission in the *ASCA* X-ray spectra of A1030 without success. For this purpose, we fit the X-ray spectrum in the region around relatively isolated, strong lines with a power-law continuum plus a Gaussian line. The redshifted line energy and width were determined from the various line contributions to each line feature. The strength of the line was allowed to vary. The fits were done using unbinned spectra and the C-statistic. For the Fe K lines, both SIS and GIS spectra were used; only the SIS spectra were fit for lower energy lines. No statistically significant line emission was detected. The 90% confidence upper limits on the equivalent widths of several strong emission lines are listed in Table 4.

We also searched for absorption lines at the redshifted wavelengths of strong, isolated allowed lines. The 90% upper limits on several absorption lines are also listed in Table 4.

## 6. DISCUSSION

### 6.1. X-ray Properties of the Quasar B2 1028+313

The total X-ray luminosity of the B2 1028+313/A1030 system was  $(0.7, 1.3, 1.7) \times 10^{45}$  erg s<sup>-1</sup> (0.2–10 keV) during the *ASCA*, *ROSAT* PSPC, and HRI observations, respectively. This is in the range of X-ray luminosities for brighter X-ray clusters, so it was possible that a significant portion of the emission is due to hot ICM, rather than the AGN. However, our observations show that the quasar dominates the X-ray properties of the system, and that X-rays from ICM make at most a small contribution to the X-ray luminosity.

The X-ray flux of B2 1028+313 varied by a factor of about two in the one year period between the *ASCA* and *ROSAT* HRI observations (Table 1). However, the *Einstein*, *ROSAT* PSPC, and *ROSAT* HRI fluxes are more nearly equal, suggesting that

such large variations may be rare, and that the higher flux (0.7–0.8  $\mu$ Jy at 1 keV) may be more typical. It is useful to compare this flux density to the core radio flux density, which is 110 mJy at 5 GHz (Gower & Hutchings 1984). The total flux at this frequency is 161 mJy (Condon et al. 1994), so that B2 1028+313 is core-dominated. Worrall et al. (1994) found a linear correlation between the X-ray and radio core fluxes of core dominated radio galaxies at redshifts  $z > 0.3$ . For the observed core radio flux of B2 1028+313, the predicted X-ray flux density at 1 keV is 0.01–0.02  $\mu$ Jy, which is a factor of at least 30 smaller than the observed flux. On the other hand, the observed X-ray flux is similar to that of lobe-dominated radio quasars with the same radio flux. This may argue that quasars and radio galaxies have a significant component to their X-ray emission which is compact and nonthermal, but not strongly beamed.

The X-ray spectra of B2 1028+313 are generally well-fit by a power-law with a photon number spectral index of  $\Gamma \approx 1.8$ , plus an excess soft X-ray component. The existing X-ray spectra do not provide a clear determination of the spectral shape of the soft component, but it can be fit by a blackbody with a temperature of about 30 eV. It contributes only about 15% of the total 0.2–10 keV X-ray luminosity of the quasar, but provides about 71% of the flux density at 0.2 keV.

In Figure 9, we show the spectral energy distribution of B2 1028+313 from the radio through the X-ray spectral band. We do not show the error bars on the points, because they are generally small and are difficult to see on the Figure. Note that the different spectral regions were observed at different epochs, and variability may affect the comparison. The X-ray flux densities are from the unfiltered *ROSAT* PSPC data and the *ASCA* data presented in this paper. Because the *ASCA* fluxes are lower than the *Einstein* or *ROSAT* fluxes (Table 1), we increased the

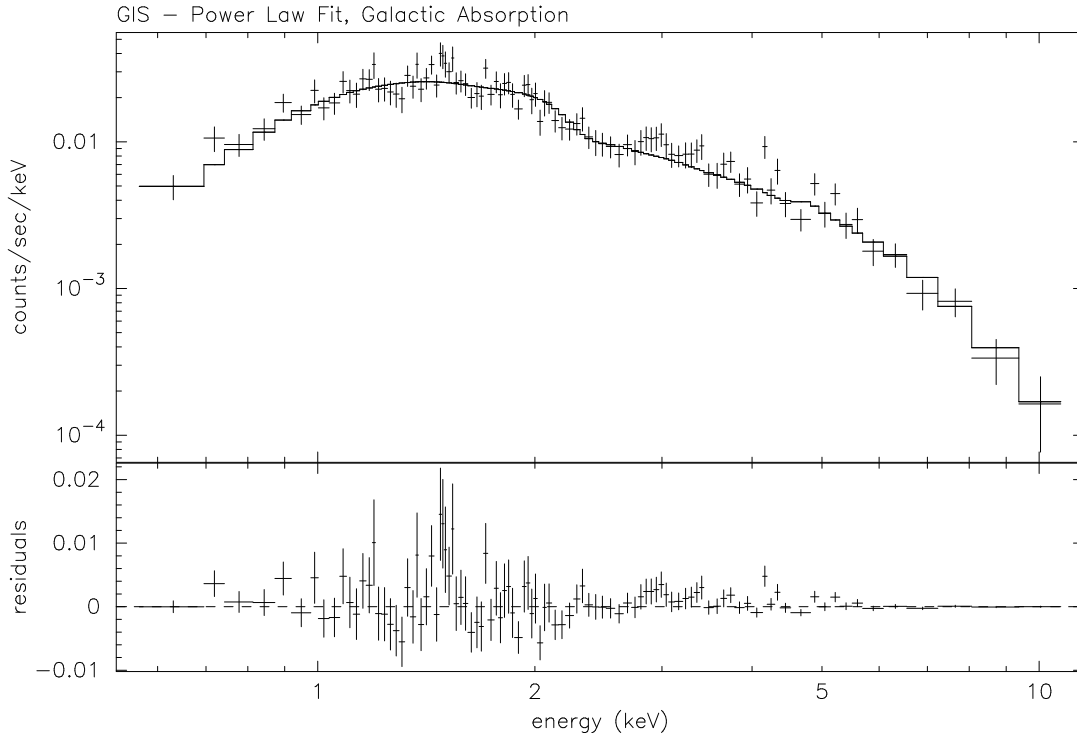


FIG. 7.— The ASCA GIS X-ray spectrum of A1030. The upper panel gives the data and the best-fit power-law model (row 7 of Table 3) assuming the measured Galactic absorption of  $N_H = 1.98 \times 10^{20} \text{ cm}^{-2}$ . The notation is the same as in Figure 5.

ASCA spectrum by a constant factor so that it agreed with the ROSAT PSPC spectrum at 1 keV. The X-ray fluxes were corrected for the response of the two instruments, and for Galactic absorption. The ASCA and ROSAT spectra were binned to reduce the errors, and averaged in the common region of spectral coverage.

The optical and UV data are taken from Koekemoer et al. (1998), and are based on HST and ground-based spectra. In order to get a measure of the continuum emission from the quasar, the flux densities were determined in wavelength regions which were free of strong emission or absorption lines. The spectrum was corrected for Galactic extinction, assuming  $A_V = 0.104$  mag, which is appropriate for the Galactic column of  $N_H = 1.98 \times 10^{20} \text{ cm}^{-2}$ . When this Galactic extinction correction is made, a broad 2200 Å absorption feature in the UV spectrum largely disappears. There is a residual feature at slightly longer wavelengths, which might be due to intrinsic absorption at the quasar redshift, additional Galactic absorption, or a very broad emission line at longer wavelengths which was not subtracted from the spectrum.

The near-IR, far-IR, and radio core fluxes are from the compilation of Elvis et al. (1994). The far-IR values, which are shown as inverted triangles in Figure 9, are upper limits. The near-IR values are fairly uncertain because of measurement errors and a significant correction for the background galaxy emission in these bands (see the discussion in Elvis et al. [1994]).

The optical and UV measurement also show a large peak in the mid-UV. This peak is crudely similar to a  $\sim 20$  eV black-

body, although the observed peak is considerably broader than a single temperature blackbody. The spectral index suggested by the near-IR data is considerably steeper than that for the hard X-ray data. This may indicate that the non-thermal spectrum flattens with increasing frequency. Alternatively, there may be a second peak in the IR spectral band. However, the uncertainties in the near-IR make it difficult to be certain about the spectrum there. The hard X-ray power-law spectrum would extrapolate to flux consistent with the highest frequency radio measurement, but it is not clear whether the radio spectrum has turned over by this point.

## 6.2. Intracluster Medium in A1030

One of the aims of this work was to determine the properties of the intracluster medium in A1030 by separating the X-ray emission of that medium from that of the quasar B2 1028+313. We had hoped to detect intracluster emission spatially (as an extended component) and spectrally (as a thermal component in the X-ray spectrum). We did detect an extended component to the X-ray emission, which was elongated to the NNW and SSW (Figures 1 and 3). However, there are several features of this emission which are inconsistent with normal ICM emission from clusters. First, it is rather highly elongated (Figure 3). Second, its radial surface brightness profile is not well-fit by either a beta-model or a cooling flow model. Third, the extended emission is quite soft, and would imply an ICM gas temperature of  $kT \approx 0.2$  keV, which is much lower than typical temperatures of  $kT \approx 7$  keV.

If we exclude the elongated X-ray features in Figure 3,

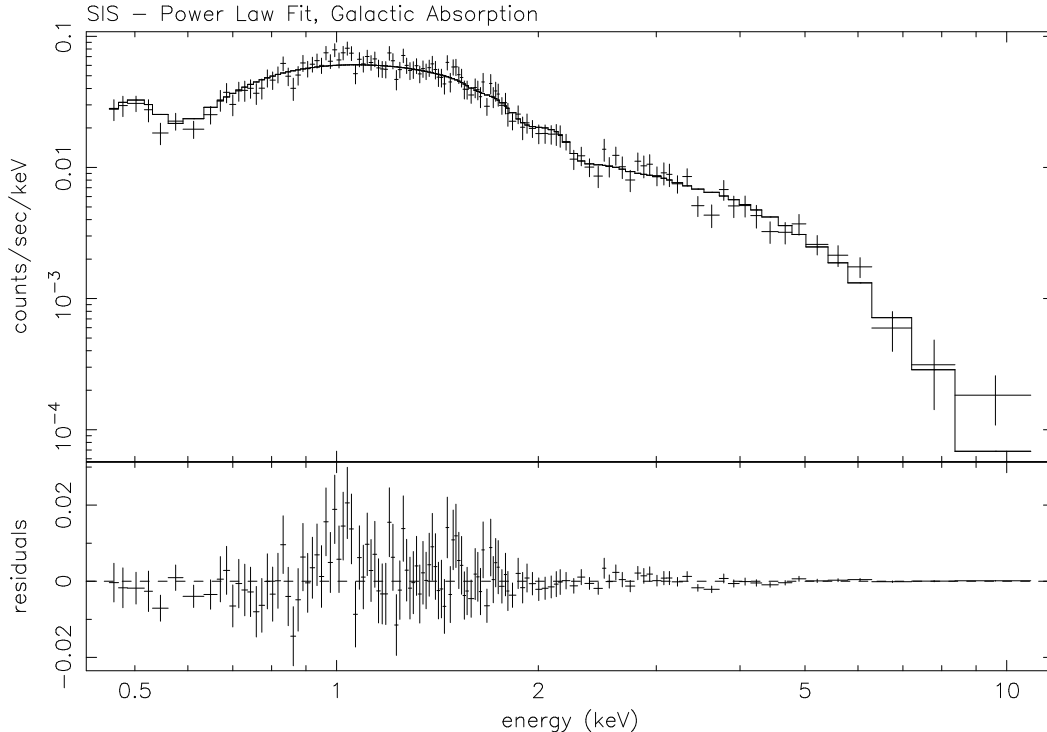


FIG. 8.— The ASCA SIS X-ray spectrum of A1030. The upper panel gives the data and the best-fit power-law model (row 10 of Table 3) assuming the measured Galactic absorption of  $N_H = 1.98 \times 10^{20} \text{ cm}^{-2}$ . The notation is the same as in Figure 5.

less than 4% of the X-ray emission in the *ROSAT* band originates in an extended component beyond a radius of  $1'$ . Of course, the brightest cluster X-ray emission may be blended into quasar emission at the center of the cluster. If A1030 had ICM with a distribution which followed a beta model (eq. 1) with  $\beta = 2/3$  and  $r_c > 150 \text{ kpc}$ , then  $>54\%$  of the ICM X-ray emission should lie at projected radii greater than  $1'$ . This suggests that  $\lesssim 8\%$  of the total X-ray emission is due to the ICM, and that an upper limit on the ICM X-ray luminosity is  $L_X(\text{ICM}) \lesssim 1.0 \times 10^{44} \text{ erg s}^{-1}$  (0.2–10 keV). For a cluster temperature of 7 keV, the corresponding limit on the central electron density, assuming the same beta model, is  $n_e \lesssim 3 \times 10^{-3} \text{ cm}^{-3}$ . The limit on the pressure of the ICM is  $P_{\text{ICM}} \lesssim 7 \times 10^{-11} \text{ dyne cm}^{-2}$ . If we adopt a lower temperature of 4 keV, which might be more appropriate given the low X-ray luminosity of the cluster, the limit on the central electron density is not affected, the limit on the X-ray luminosity is 20% lower, and the limit on the central pressure is  $P_{\text{ICM}} \lesssim 4 \times 10^{-11} \text{ dyne cm}^{-2}$ .

The X-ray spectra do not require any ICM thermal component. The upper limits on the X-ray luminosity of a thermal component with a heavy element abundance of 0.3 of solar and a typical cluster temperature of  $kT = 7 \text{ keV}$  is  $L_X < 1.5 \times 10^{44} \text{ erg s}^{-1}$ . In addition to limits based on overall fits to the spectrum, we also searched for strong iron, silicon, and sulfur emission lines from the ICM. None were found; the limits on the equivalent width are consistent with but somewhat weaker than the limits on X-ray luminosity based on the integrated spectrum, assuming typical cluster abundances. We also placed limits on the cooling rate of any central cooling flow component. The upper limit, making the same assumptions about abundances and the initial temperature, is  $\dot{M} < 93 M_\odot \text{ yr}^{-1}$ .

These limits on the ICM X-ray luminosity do not require that A1030 be unusually faint for an Abell richness 0 cluster. The upper limit is at the high end of the X-ray luminosities observed for richness 0 clusters at redshifts below 0.25 (e.g., Rosati et al. 1998).

### 6.3. Extended X-ray Emission and Radio Source

The elongation of the extended X-ray emission in A1030 is along the same direction as the extended radio emission. On small scales ( $r \lesssim 5''$ ), the radio image of B2 1028+313 shows a bright core and a jet propagating to the north at a position angle of about  $-30^\circ$  (Gower & Hutchings 1984). On larger scales, radio lobes are seen to the NNW and SSE. While the orientation varies somewhat with radius between position angles of about  $-45^\circ$  and  $0^\circ$  to the north, and about  $130^\circ$  and  $170^\circ$  to the south, overall the orientation is along position angles of about  $-30^\circ$  and  $150^\circ$  (Owen, White, & Ge 1993; Owen & Ledlow 1997). The largest scale radio emission is most useful for comparison to the X-ray emission. On scales comparable to the size of the extended X-ray emission in the *ROSAT* PSPC image (Figure 3), the best radio image may be provided by the NVSS survey (Condon et al. 1998).

Figure 10 shows contours of the *ROSAT* image superposed on a greyscale representation of the NVSS 20 cm radio images. The NVSS image has a resolution of  $45''$ . The radio source to the east is almost certainly an unrelated background source. At radii of  $1\text{--}2'$ , the radio emission is elongated in nearly the same direction as the X-ray emission. It is not clear whether the radio emission continues to larger radii; if one extrapolates the observed radial surface brightness trend to larger radii, the emission might be expected to be below the noise in the NVSS

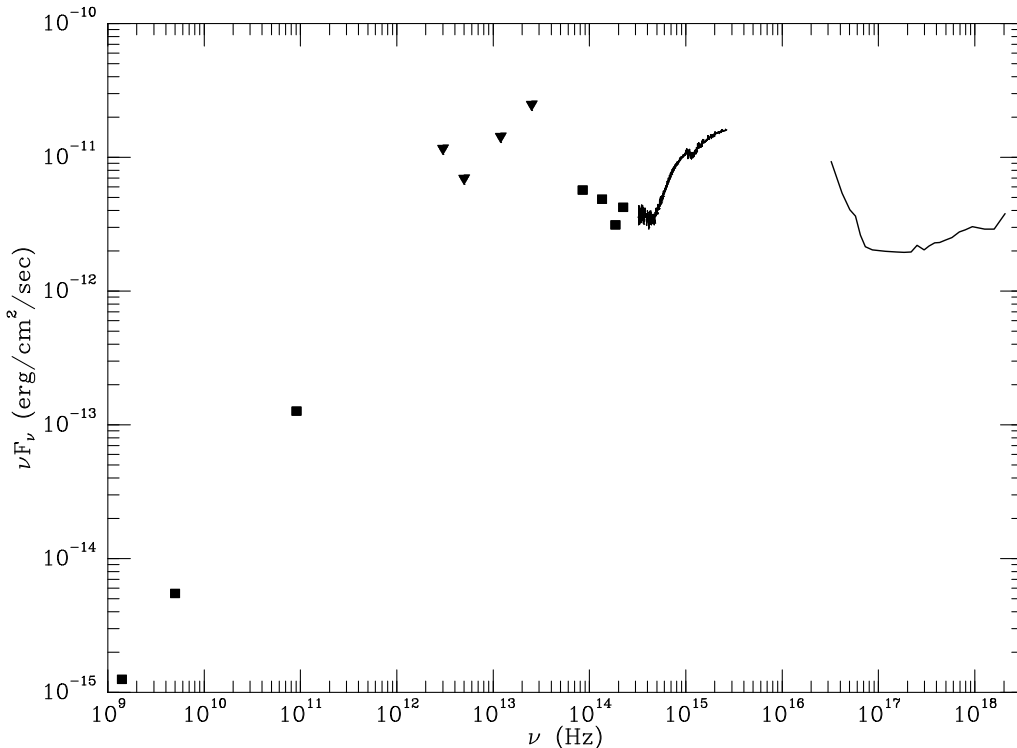


FIG. 9.— The spectral energy distribution of B2 1028+313. The frequency times the flux density,  $\nu F_\nu$  is plotted versus the frequency as observed. The X-ray flux densities are from the unfiltered *ROSAT* PSPC data and the *ASCA* data, both corrected for Galactic absorption and instrumental sensitivity. The optical and UV data are taken from the composite *HST* and ground-based spectrum in Koekemoer et al. (1998). Emission and absorption line free regions were used to determine this spectrum, which is corrected for Galactic extinction. The near-IR, far-IR, and radio core fluxes are from the compilation of Elvis et al. (1994). The far-IR values, which are shown as inverted triangles, are upper limits.

image.

The total flux density of the radio source is 254 mJy at 20 cm (Owen & Ledlow 1997). In the NVSS image, 215 mJy of emission is due to unresolved emission from the central source, leaving a total of 39 mJy of possible extended emission on the scale of the 45'' beam of the survey. The fluxes in the northern and southern extensions on the NVSS image in Figure 10 are about 5.4 and 7.4 mJy, respectively.

Extended emission is also seen at lower frequencies in the 49 cm WENSS survey image of this region (Rengelink et al. 1997). Although the noise level is higher and the beam larger than in the NVSS survey, the WENSS image shows north and south lobes at the same locations as in the NVSS image. The flux densities of the northern and southern lobes at 49 cm are 22.5 and 20.3 mJy, respectively. Because of differences in the resolution, it is unclear whether the NVSS and WENSS fluxes correspond to identical regions. To reduce somewhat the uncertainties, we will sum the emission from the two lobes in each of the instruments. Assuming they come from the same region, the ratio of fluxes implies an energy spectral index in the radio of  $\alpha = 1.45 \pm 0.30$  (a photon number spectral index of  $\Gamma = 2.45 \pm 0.30$ ), where the error estimate follows from the different values for the northern and southern lobes. This is similar to, but not quite as steep as, the spectral index suggested by the X-ray colors of the extended emission (§ 4.2). Given the fluxes, size, and spectral index, we can estimate the properties of the radio source under the minimum energy assumption (e.g., Miley 1980). We assumed that the relativistic electrons and ions

had equal energies, that the radio plasma filled the observed emitting volume, and that the magnetic field was transverse to the line of sight. The radio spectrum of each component was assumed to be a power law from a frequency of 10 MHz to 100 GHz. We assumed that the observed lobes were cylinders whose axis is perpendicular to our line of sight. The implied magnetic field strength was  $B \approx 1.6 \mu\text{G}$ , the nonthermal pressure was  $P_{\text{rad}} \approx 1.5 \times 10^{-13} \text{ dyne cm}^{-2}$ , and the total energy in the lobes was about  $1.6 \times 10^{59} \text{ erg}$ . The lifetime of the electrons which emit at 1.4 GHz is about  $4 \times 10^7 \text{ yr}$ , which is probably an upper limit to the age of the radio source.

What is the source of the elongated X-ray emission which is extended along the radio structure in Figure 10? One possibility is that the radio lobes are interacting with intracluster gas, and have compressed the gas. In this case, the enhanced X-ray emission would be expected around the perimeter of the radio lobes. The X-ray and radio spatial resolutions in Figure 10 are too poor to provide a useful test of this predictions. If the radio lobes compressed the surrounding intracluster gas (either adiabatically or in shocks), the gas would have been heated. Actually, the X-ray emission from the X-ray extensions is quite soft (§ 4.2), corresponding to a gas temperature of about 0.2 keV. Thus, this model requires that the compressed gas cool to low temperatures. No evidence of cooling emission is seen in the spectrum of the source (§ 5.3). The compressed gas would have to be dense enough to cool within the lifetime of the radio source, which would require that  $n_e \gtrsim 0.1 \text{ cm}^{-3}$ . If the intracluster gas were compressed by strong shocks, its density would

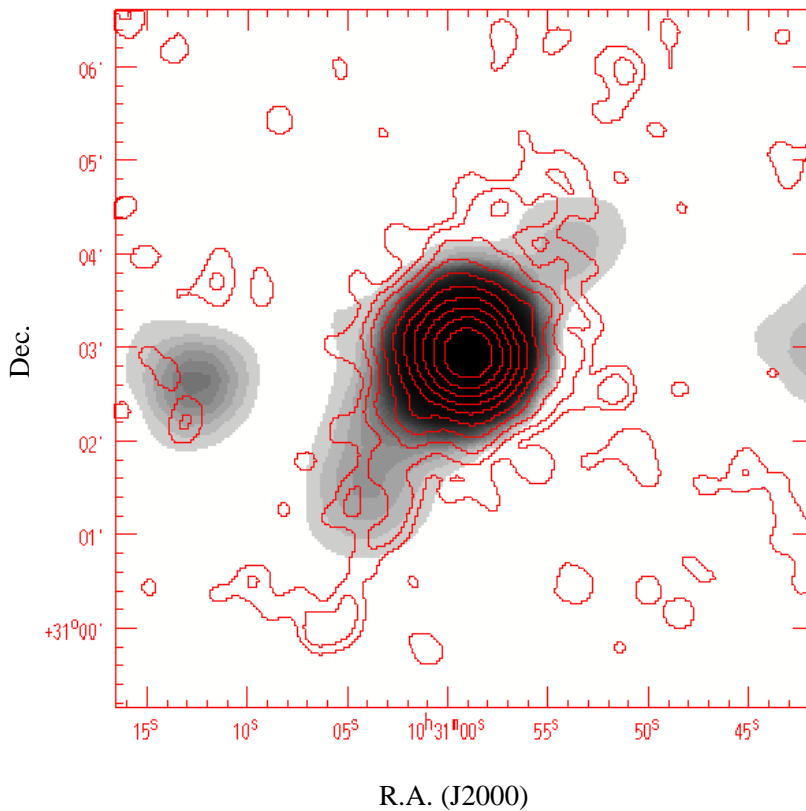


FIG. 10.— Contours of the central *ROSAT* PSPC X-ray image of A1030 are shown superposed on a greyscale representation of the NVSS 20 cm radio image. The greyscale for the radio ranges from about 1 to 205 mJy/beam. The *ROSAT* image and contours levels are the same as those in Figure 3.

only increase by a factor of 4 until cooling was effective. Thus, the ambient gas density in the region around the radio source must exceed  $2 \times 10^{-2} \text{ cm}^{-3}$  for this model to work. The upper limit on the gas density at the radii of the radio lobes based on the upper limit of the X-ray surface brightness at these radii away from the radio source is  $n_e \lesssim 1 \times 10^{-3} \text{ cm}^{-3}$ . Thus, it is unlikely that such gas could cool rapidly enough to produce the regions of enhanced soft X-ray emission.

Alternatively, the X-ray emission may be due to cooler gas which is falling into the central galaxy in A1030, either alone or as part of the merger of a gas-rich galaxy with the central cD. West (1994) suggested that such mergers onto cD galaxies will mainly occur along filaments in the large-scale structure surrounding the cluster, and that they will produce cD galaxies which are prolate in shape. West argued that gas which falls into such a galaxy will form a disk with its rotation axis being parallel to the major axis of the cD galaxy. The extended X-ray emission in A1030 is elongated at an angle of about  $70^\circ$  from the major axis of the host galaxy of B2 1028+313, which is at a position angle of  $45^\circ$  (Ledlow & Owen 1995). Thus, this might be consistent with West's scenario. However, West also argues that the gaseous accretion disk will determine the axis of the central radio jets, which should be perpendicular to the major axis of the gas disk and parallel to the optical major axis of the galaxy. This gives the wrong relative orientations of the gas disk and radio source and of the optical galaxy and radio source for B2 1028+313.

Finally, the extended X-ray emission might be due to Inverse Compton (IC) scattering of Cosmic Microwave Background (CMB) photons by low energy cosmic ray electrons from the

radio lobes. As noted above (§ 4.2), the extended emission has a very soft X-ray color, which is consistent with a steep power-law X-ray spectrum ( $\Gamma = 2.9 \pm 0.4$ ). We have calculated the expected ratio of the IC X-ray flux to the synchrotron radio fluxes using the general expressions for the IC and synchrotron emission from power-law electron energy distributions (Blumenthal & Gould 1970; Sarazin 1988). The ratio of the IC flux at a frequency  $\nu_X$  to the synchrotron flux at a frequency  $\nu_r$  is

$$\frac{f_{IC}(\nu_X)}{f_{syn}(\nu_r)} = \frac{2\pi e}{h^2 c^4 m_e B_\perp} \frac{b(p)}{a(p)} (kT_{CMB})^3 (1+z)^{3+\alpha} \times \left( \frac{4\pi m_e c k T_{CMB}}{3heB_\perp} \right)^\alpha \left( \frac{\nu_r}{\nu_X} \right)^\alpha, \quad (3)$$

where  $T_{CMB} = 2.73 \text{ K}$  is the temperature of the CMB radiation at zero redshift,  $B_\perp$  is the component of the magnetic field in the radio source perpendicular to our line of sight,  $p = 2\alpha + 1$  is the power-law index of the electron energy distribution, and  $a(p)$  and  $b(p)$  are two analytic functions of  $p$ , which are given in equations (5.8) and (5.6) in Sarazin (1988). The power-law electron energy distribution was determined from the radio flux and spectral index  $\alpha = 1.45$  of the radio lobes, assuming that the electrons were fit by a single power-law distribution. Given the radio fluxes of the two lobes, the radio spectral index, and assuming a magnetic field of  $B_\perp = 1 \mu\text{G}$ , the total predicted IC flux density from both of the lobes is  $0.3 \mu\text{Jy}$  at  $0.2 \text{ keV}$ , which is about a factor of two smaller than the observed total flux of both lobes. Because of the uncertainties in all these numbers, it is possible that the extended X-ray emission may be inverse Compton emission associated with the radio source. The IC

soft X-ray emission might also be enhanced by scattering of the radio emission from the quasar, particularly if part of that emission is beamed in the same direction as the radio beams. If the spectral energy distribution of the quasar (Figure 9) is extrapolated to the peak of the CMB spectrum, one estimates that the brightness temperature of the radio source is about 1 K at a distance corresponding to a projected radius of  $1'$  from the nucleus. Thus, the local radiation field probably does increase the IC flux somewhat. One concern with the IC model is that one might expect a more exact correspondence between the extended X-ray and radio features in Figure 10. On the other hand, the differences might be due to the low spatial resolution and signal to noise ratio of both the X-ray and radio images, or to differences between the distributions of the low energy cosmic rays which produce the IC X-rays and the higher en-

ergy particles which produce the synchrotron radio emission. Another concern with the IC model is that it requires that the same very steep spectral index for the radio lobes apply down to very low frequencies, since the electrons which produce the IC soft X-ray emission have much lower energies than those which produce the radio emission.

We thank Dan Harris, Jonathon Silverman, and the referee, Patrick Hall, for useful comments. C. L. S. was supported in part by NASA ROSAT grants NAG 5-3308, NAG 5-4787, NASA ASCA grant NAG 5-2526, and NASA Astrophysical Theory Program grant 5-3057. Partial support for this work was provided by NASA through grant number GO-05934.01-94A from the STScI, which is operated by AURA, under NASA contract NAS5-26555.

## APPENDIX

### CORRECTION OF HRI IMAGE FOR ASPECT ERRORS

During pointed observations with *ROSAT*, the satellite is normally “wobbled” by several arcmin with a period of several hundred seconds. The result of this wobbling is that photons from a given location on the sky are collected over an elongated regions of the detector. Figure 11 shows the detector coordinate positions of photons from the center of the image of A1030. The elongation at  $PA \approx 45^\circ$  is due to the wobble. The image is reconstructed by determining the pointing direction of the satellite at the arrival time of each of the photons. Morse (1994) suggested that errors in this aspect solution during the wobble can result in extended and elongated images of point sources. (Note that Morse finds that the observed elongations of the images of point sources aren’t necessarily in the same direction as the projection of the wobble on the sky, although the elongations are still due to wobble-dependent aspect errors.)

Morse argued that aspect errors were correlated with the phase of the wobble, and they might be corrected by registering subimages collected as a function of the wobble phase. He suggested that subimages be collected from small regions of the detector. Because the extension of a point source in detector coordinates is mainly due to the wobble, this is nearly equivalent to selecting photons at the same phase in the wobble. Morse suggested that regions which were  $5'' \times 5''$  be used. The subimages must contain at least 100 photons to allow the centroid of each to be determined with sufficient accuracy. Even if larger detector regions of  $10'' \times 10''$  are used, there will typically be  $\gtrsim 100$  such subimages. Thus, this technique requires that the central source in the image contain  $\gtrsim 10^5$  photons. We attempted to correct our image for A1030 using the FTOOLS HRIASPCOR implementation of Morse’s algorithm. Unfortunately, the central region of our image of A1030 contained about 3000 counts, including background. We found that this was too few counts to apply Morse’s algorithm in its original form. The HRIASPCOR program produced a highly elongated and irregular image.

We developed a minor variant of the Morse algorithm, which can be applied to somewhat fainter sources. (Recently, we found that a similar technique has been used previously by Hall et al. [1995]. Also, as this paper was being revised, we learned of a new technique for improving the aspect solution of HRI images, which is presented in Harris, Silverman, & Hasinger [1998]. In principle, this new technique should work even better than the previous ones, including the one presented here, for relatively faint sources.) Because the wobble is mainly in a single direction, we collect photons into subimages within the detector using long, narrow rectangle regions. The longer side of these rectangular regions is perpendicular to the direction of the wobble. Figure 11 shows the 13 rectangular regions we used to correct the image of A1030. The regions are  $20''$ , except for the two at the ends of the wobble which are  $40''$  wide. We constructed subimages using photons collected from each of these detector regions, determined their centroids, and registered them to a common centroid. The resulting image of the center of A1030 is shown in Figure 1b. The center part of this image is narrower than the original image (Fig. 1a).

One concern with the Morse procedure is that registering subimages of an image will always produce a more compact image, even if the subimages are randomly sampled from the original image. As an extreme example, if the number of subimages equals the number of photons, then the resulting corrected image will be a delta function, whatever the distribution of the original photons. In general, if an image contains  $N$  photons with a gaussian distribution, and the image is subsampled randomly into  $m$  subimages each containing  $(N/m)$  photons, then the dispersion of the gaussian distribution will be artificially reduced by a factor of  $[(N-m)/(N-1)]^{1/2}$ . In our case,  $N \approx 3000$  and  $m = 13$ , so this should not be an important effect. We have verified this by creating random subimages of our image, and we find that they are not significantly different from the original image, and are not as centrally condensed as the wobble-corrected image in Figure 1b. A second worry is that the distribution of photons on the detector is a convolution of the wobble and the actual spatial distribution of photons on the sky. As a result, registering the subimages artificially reduces the extent of the resulting image. However, this effect depends on the ratio of the size of the image on the sky ( $\sim 10''$  for the central part of the A1030 image) to the size of the wobble ( $\sim 5'$  in Figure 11), and thus is expected to be quite small.

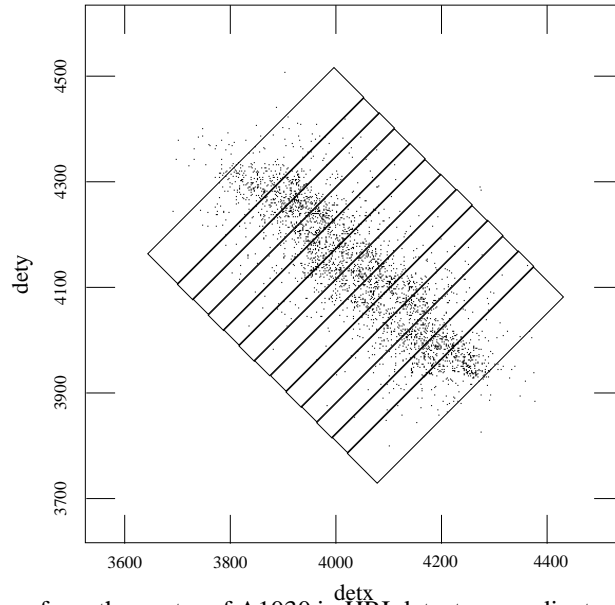


FIG. 11.— The image of photons from the center of A1030 in HRI detector coordinates. The elongation of the image at a position angle of about  $45^\circ$  is due to the “wobbling” of the telescope. The rectangles show the regions of the detector used to collect subimages at different phases of the wobble.

#### REFERENCES

- Abell, G. O., Corwin, J., H. G., & Olowin, R. P. 1989, *ApJS*, 70, 1  
 Blumenthal, G. R., & Gould, R. J. 1970, *RMP*, 42, 237  
 Blumenthal, G. R., Keel, W. C., & Miller, J. S. 1982, *ApJ*, 257, 449  
 Condon, J. J., Broderick, J. J., Seielstad, G. A., Douglas, K., & Gregory, P. C. 1994, *AJ*, 107, 1829  
 Condon, J. J., Cotton, W. D., Greisen, E. W., Yin, Q. F., Perley, R. A., Taylor, G. B., & Broderick, J. J. 1998, preprint  
 David, L. P., Harnden, F. R., Kearns, K. E., & Zombeck, M. V. 1993, *The ROSAT High Resolution Imager (HRI)*, (Cambridge: Smithsonian Astrophysical Observatory)  
 Elvis, M., Lockman, F. J., & Wilkes, B. J. 1989, *AJ*, 97, 777  
 Elvis, M., Wilkes, B. J., & Tannabaum, H. 1985, *ApJ*, 292, 357  
 Elvis, M., et al. 1994, *ApJS*, 95, 1  
 Fabian, A. C. 1994, *ARA&A*, 32, 277  
 Gower, A. C., & Hutchings, J. B. 1984, *AJ*, 89, 1658  
 Hall, P. B., Ellingson, E., Green, R. F., & Yee, H. K. C. 1995, *AJ*, 110, 513  
 Harris, D. E., Silverman, J. D., & Hasinger, G. 1998, in preparation  
 Heckman, T. M., Baum, S. A., van Breugel, W. J. M., & McCarthy, P. 1989, *ApJ*, 338, 48  
 Idesawa, E., et al. 1997, preprint ([ftp://legacy.gsfc.nasa.gov/asca/gis\\_information/gain.gs.gz](ftp://legacy.gsfc.nasa.gov/asca/gis_information/gain.gs.gz))  
 Jackson, N., & Browne, I. W. A. 1991, *MNRAS*, 250, 414  
 Koekemoer, A. M., O’Dea, C. P., Baum, S. A., Sarazin, C. L., Owen, F. N., & Ledlow, M. J. 1998, *ApJ*, submitted  
 Lanzetta, K. M., Turnshek, D. A., & Sandoval, J. 1993, *ApJS*, 84, 109  
 Ledlow, M. J., & Owen, F. N. 1995, *AJ*, 110, 1959  
 Masnou, J. L., Wilkes, B. J., Elvis, M., McDowell, J. C., & Arnaud, K. A. 1992, *A&A*, 253, 35  
 Miley, G. 1980, *ARA&A*, 18, 165  
 Morse, J. A. 1994, *PASP*, 106, 675  
 Owen, F. N., & Ledlow, M. J. 1997, *ApJS*, 108, 41  
 Owen, F. N., Ledlow, M. J., & Keel, W. C. 1995, *AJ*, 109, 14  
 Owen, F. N., Ledlow, M. J., & Keel, W. C. 1996, *AJ*, 111, 53  
 Owen, F. N., Ledlow, M. J., & Keel, W. C. 1998, in preparation  
 Owen, F. N., White, R. A., & Ge, J.-P. 1993, *ApJS*, 87, 135  
 Plucinsky, P. P., Snowden, S. L., Briel, U. G., Hasinger, G., & Pfeffermann, E. 1993, *ApJ*, 418, 519  
 Rengelink, R. B., Tang, Y., de Bruyn, A. G., Miley, G. K., Bremer, M. N., Röttgering, H. J. A., & Bremer, M. A. R., 1997, *A&AS*, 124, 259  
 Rosati, P., Della Ceca, R., Norman, C., & Giacconi, R. 1998, *ApJ*, 492, L1.  
 Sarazin, C. L. 1988, *X-ray Emission from Clusters of Galaxies* (Cambridge: Cambridge Univ. Press), 136  
 Sarazin, C. L. 1989, *ApJ*, 345, 12  
 Shastri, P., Wilkes, B. J., Elvis, M., & McDowell, J. 1993, *ApJ*, 410, 29  
 Snowden, S. L. 1995, *Cookbook for Analysis Procedures for ROSAT XRT/PSPC Observations of Extended Objects and the Diffuse Background* (Greenbelt: NASA USRSDC)  
 West, M. J. 1994, *MNRAS*, 268, 79  
 Wilkes, B. J., & Elvis, M. 1987, *ApJ*, 323, 243  
 Wise, M. W., & Sarazin, C. L. 1997, in *X-ray Imaging and Spectroscopy of Cosmic Hot Plasmas*, ed. by F. Makino & K. Mitsuda (Tokyo: Universal Academy Press), 133  
 Worrall, D. M., Lawrence, C. R., Pearson, T. J., & Readhead, A. C. 1994, *ApJ*, 420, L17.  
 Yee, H. K., & Ellingson E. 1993, *ApJ*, 411, 43  
 Zamorani, G., et al., 1981, *ApJ*, 245, 357  
 Zhou, Y. Y., & Yu, K. N. 1992, *ApJ*, 400, 430